



# Unraveling the discriminative mechanisms for peroxy activation via atomically dispersed Fe-N<sub>5</sub> sites for tunable water decontamination

Xinyu Song<sup>a,b</sup>, Yang Shi<sup>a</sup>, Zelin Wu<sup>a,b</sup>, Bingkun Huang<sup>a,b</sup>, Xinhao Wang<sup>a,b</sup>, Heng Zhang<sup>a,b</sup>, Peng Zhou<sup>a,b</sup>, Wen Liu<sup>c</sup>, Zhicheng Pan<sup>d</sup>, Zhaokun Xiong<sup>a,b,c,\*</sup>, Bo Lai<sup>a,b,\*</sup>

<sup>a</sup> State Key Laboratory of Hydraulics and Mountain River Engineering, College of Architecture and Environment, Sichuan University, Chengdu 610065, China

<sup>b</sup> Sino-German Centre for Water and Health Research, Sichuan University, Chengdu 610065, China

<sup>c</sup> The Key Laboratory of Water and Sediment Sciences, Ministry of Education, College of Environmental Sciences and Engineering, Peking University, Beijing 100871, PR China

<sup>d</sup> Water Safety and Water Pollution Control Engineering Technology Research Center in Sichuan Province, Haitian Water Group, China

## ARTICLE INFO

### Keywords:

Fenton-like reactions

Single-atom catalyst

Radical and nonradical pathways

Practical application

## ABSTRACT

The discriminative activities and mechanisms for activation of O-O bond in peroxy compounds via single-atom catalysts (SACs) especially with a higher coordination number (M-N<sub>5</sub>) are rarely explored. Herein, the atomic catalyst (Fe-SAC) with Fe-N<sub>5</sub> as the active center was constructed, which could simultaneously and effectively activate peroxymonosulfate (PMS), peroxydisulfate (PDS), and hydrogen peroxide (H<sub>2</sub>O<sub>2</sub>). Density functional theory (DFT) calculations combined with experiments results demonstrated that the degradation efficiencies of acyclovir were corresponding to the changes of O-O bond length in various peroxy compounds. Meanwhile, the experiments exposed that the three oxidants all produced <sup>•</sup>OH, but the PMS also contained <sup>1</sup>O<sub>2</sub> and Fe(IV)=O, and PDS contained O<sub>2</sub><sup>•−</sup> additively. The scale-up experiment showed Fe-SAC could operate steadily for nearly 7 d. Overall, this work unveils the discriminative mechanisms for activation of O-O band in different Fenton-like systems. Moreover, the Fe-SAC with high coordination numbers has excellent catalytic properties and practical performance.

## 1. Introduction

In recent decades, peroxymonosulfate (PMS), peroxydisulfate (PDS), and hydrogen peroxide (H<sub>2</sub>O<sub>2</sub>) are the common oxidants of Fenton-like reactions [1]. H<sub>2</sub>O<sub>2</sub> is the most environmentally friendly oxidant. Nevertheless, it has storage and transportation ventures and low utilization efficiency [2–4]. Based PMS or PDS is not austere dependent on solution pH and more convenient for transportation and storage compared with H<sub>2</sub>O<sub>2</sub>, whereas uneconomical in pragmatic application [5–7]. All three oxidants contain peroxide (O-O) bonds similarly, and the bond lengths of PMS, PDS, and H<sub>2</sub>O<sub>2</sub> are 1.460, 1.497, and 1.453 Å, respectively [8–11]. O-O band can activate via energy and electron transfer reactions, moreover the breaking mode of O-O band is closely related to the reaction mechanism [6,8,9,12,13]. Accordingly, researching and comparing the mechanisms of O-O band activation in the Fenton-like reactions is greatly essential for unraveling the mechanisms. Both radical and nonradical pathways exist in Fenton-like

reactions [14]. On the one hand, they can generate a higher yield of various reactive oxygen species (ROS), for instance, hydroxyl radical (<sup>•</sup>OH), superoxide radical (O<sub>2</sub><sup>•−</sup>) or sulfate radical (SO<sub>4</sub><sup>•−</sup>). And on the other hand, they can degrade contaminants by singlet oxygen (<sup>1</sup>O<sub>2</sub>), electron-transfer pathway (ETP), or high valent metal-oxo species [15–28]. PMS was usually readily decomposed into <sup>•</sup>OH and SO<sub>4</sub><sup>•−</sup> after accepting electrons from catalysts [6,29–35]. Besides PMS could also produce PMS anion radical (SO<sub>5</sub><sup>•−</sup>) engaging as an electron donor to yield <sup>1</sup>O<sub>2</sub> [36]. PDS could gain electrons from the central metal atom to form SO<sub>4</sub><sup>•−</sup>, which was further converted to <sup>•</sup>OH or <sup>1</sup>O<sub>2</sub> [13,17,20]. Moreover, the catalysis of H<sub>2</sub>O<sub>2</sub> often required a lower pH value and <sup>•</sup>OH was the only active substance [25].

Single-atom catalysts (SACs) can efficiently catalyze diverse oxidants to treat organic pollutants. SACs as heterogeneous catalysts have prominent recyclability and stability contrasting with homogeneous systems. Moreover, SACs maximize the metal atom utilization and possess tunable electronic structures, resulting in significant catalytic

\* Corresponding authors at: State Key Laboratory of Hydraulics and Mountain River Engineering, College of Architecture and Environment, Sichuan University, Chengdu 610065, China

E-mail addresses: [scuxzk@scu.edu.cn](mailto:scuxzk@scu.edu.cn) (Z. Xiong), [laibo@scu.edu.cn](mailto:laibo@scu.edu.cn) (B. Lai).

<https://doi.org/10.1016/j.apcatb.2023.123240>

Received 11 July 2023; Received in revised form 19 August 2023; Accepted 27 August 2023

Available online 28 August 2023

0926-3373/© 2023 Elsevier B.V. All rights reserved.

activity [36–38]. Qian et al. constructed Fe single-atom structures on a carbon nanotube to degrade bisphenol A by activating PMS [16]. Single-atom  $\text{CoN}_{2+2}$  site could activate PMS to  $^1\text{O}_2$  with almost 100% conversion [39]. A single-atom Cu catalyst generated the high-valent copper species Cu(III) with PDS for elective degradation of electron-rich pollutants [18]. Zhang and co-workers fabricated a single-atom-Fe(III) catalyst for PDS activation, that degraded pollutants by nonradical oxidation [40]. On the other hand, copper single-atoms were fastened to a thiol-functionalized water treatment membrane, which could activate  $\text{H}_2\text{O}_2$  to generate hydroxyl radicals for effective acetaminophen degradation during filtration [41]. Therefore, the related research about SACs was rapidly growing as a hot spot.

In the present study, most SACs focused on metal- $\text{N}_4$  coordination [39,42–45], and the coordination number of a single atom can significantly affect its catalytic performance [46]. Meanwhile, a small part was metal- $\text{N}_3$  [47], however, SACs with low coordination numbers would reduce oxidation activity and may higher energy barrier to regenerate the active site [48,49]. SACs with more than four coordination were researched rarely, only a few pieces of literature researched metal- $\text{N}_5$  single atomic materials and all were persulfate systems in advanced oxidation processes (AOPs). Besides, the catalytic performance and discriminative mechanisms for different oxidants activation via atomically dispersed Fe- $\text{N}_5$  sites are still lacking.

Inspired by these excellent works abovementioned, the study constructed a high-coordination single atomic catalyst that possessed specific Fe- $\text{N}_5$  sites. Meantime, the catalyst overcame the common weaknesses of single-atomic catalysts such as poor recycling performance and high metal dissolution. Firstly, density functional theory (DFT) was used to calculate adsorption energy, changes of O-O bond lengths, and the electron transfers between the active site and the oxidant. The consequences interpreted the adsorption evolutionary process of each oxidant and indicated PMS/Fe-SAC system had the most efficient for oxidation. And then the basic experiment was conducted that showed the Fe- $\text{N}_5$  had a predominant activation effect on three oxidants (PMS,  $\text{H}_2\text{O}_2$ , PDS) at the same time. Afterward, combining the results of the theoretical calculation with experiments, we can unravel the discriminative mechanisms for peroxy activation.

## 2. Materials and methods

### 2.1. Chemical reagents

Acyclovir (ACV, AR, >99%), potassium peroxymonosulfate (PMS), sodium persulfate (PDS), dicyandiamide ( $\text{C}_2\text{H}_4\text{N}_4$ ), trimesic acid ( $\text{C}_9\text{H}_6\text{O}_6$ ), furfuryl alcohol (FFA), nitrotertrazolium blue chloride (NBT), isopropanol (IPA), coumarin, 7-hydroxycoumarin, humic acid (HA), sodium chloride (NaCl) and potassium chloride (KCl) were purchased from Shanghai Aladdin reagent Inc. Methyl phenyl sulfoxide (PMSO), methyl phenyl sulfone (PMSO<sub>2</sub>), dimethyl sulfoxide (DMSO), sodium bicarbonate ( $\text{NaHCO}_3$ ) were purchased from Shanghai Macklin Biochemical Co., Ltd. Sodium sulfate ( $\text{Na}_2\text{SO}_4$ ), sulfuric acid ( $\text{H}_2\text{SO}_4$ ), sodium hydroxide (NaOH), *p*-benzoquinone (*p*-BQ), tert-butanol (TBA), hydrogen peroxide ( $\text{H}_2\text{O}_2$ , AR, 30%), iron (II) chloride tetrahydrate ( $\text{FeCl}_2 \cdot 4 \text{H}_2\text{O}$ ), sodium thiosulfate ( $\text{Na}_2\text{S}_2\text{O}_3$ ), potassium phosphate monobasic ( $\text{KH}_2\text{PO}_4$ ), potassium bicarbonate ( $\text{KHCO}_3$ ), methyl alcohol (MeOH) and potassium thiocyanate (KSCN) were purchased from Chengdu Kelong chemical reagent factory. Sodium dihydrogen phosphate ( $\text{NaH}_2\text{PO}_4$ ) was purchased from GENERAL-REAGENT. In the experiment, all chemical reagents were of analytical grade and used directly without further purification. Deionized water was used throughout the experiment.

### 2.2. Synthesis of catalytic materials

As a typical synthesis, 164 mg  $\text{FeCl}_2 \cdot 4 \text{H}_2\text{O}$  was mixed with dicyandiamide (15 g) and trimesic acid (1.5 g), fully grinding and

mixing until the mixed precursor would change into uniform color evenly, then annealed in an argon atmosphere at 800 °C, and the heating rate was 5 °C/min. After 3 h of pyrolysis, the as-obtained black sample was ground and named Fe-SAC. Nitrogenated carbon (NC) as a reference was obtained by a simple thermal polycondensation method without the addition of  $\text{FeCl}_2 \cdot 4 \text{H}_2\text{O}$ .

### 2.3. Catalytic degradation of pollutants

ACV as a representative antiviral drug has extensive production and application possessed aroused growing attention. Therefore, ACV was taken as the target pollutant in this study. At each reaction, 100 mL ACV solution (2 mg/L) was added to a 250 mL glass beaker with a mechanical agitation rate of 300 rpm at  $25 \pm 1$  °C. The dosage of the catalyst was 150 mg/L, and the concentrations of PMS, PDS, and  $\text{H}_2\text{O}_2$  were 0.5 mM, 0.5 mM, and 10 mM, respectively. Samples were extracted at pre-determined intervals and filtered with 0.22 μm PTFE syringe filter discs, then mixed with 30 μL  $\text{Na}_2\text{S}_2\text{O}_3$  (0.1 M) for quenching. All experiments were repeated two or three times, all points in the figures were the average of the results and the error bars represent the standard deviation of the average.

### 2.4. Analytical methods

The morphology of Fe-SAC was investigated using transmission electron microscope (TEM, Talos F200S G2). Aberration-corrected high-angle annular dark-field scanning transmission electron microscopy (AC-HAADF-STEM) and the corresponding energy-dispersive X-ray spectroscopy (EDX) mapping image of Fe were recorded on a JEOL JEM-ARM200F STEM/TEM (Japan). Fe K-edge X-ray absorption fine structure (XAFS) analyses were performed with Si (111) crystal monochromators at the BL14W Beamline at the Shanghai Synchrotron Radiation Facility (SSRF, Shanghai, China) to gain insights into the single-atom Fe sites at the atomic level. X-ray photoelectron spectroscopy (XPS) measurements were performed on the Thermo Scientific ESCALAB 250Xi spectrometer (USA) using an Al Kα X-ray source with pass energy of 200.0 eV. The content of metal ions was detected by inductively coupled plasma atomic emission spectroscopy (Agilent ICP-OES 5110). The concentration of leached iron was quantified by graphite furnace atomizer atomic absorption spectrophotometry (GFA-6880; AA-6880, Shimadzu). The details of the DFT calculations were shown in Text S1. The concentration of target organics (ACV) was measured using high-performance liquid chromatography (HPLC, LC-16, SHIMAZU) equipped with an InertSustain C18 separation column ( $4.6 \times 250$  mm) and a UV detector. The mobile phase was a mixture of methanol and water ( $V/V = 80/20$ ) with a flow rate of 1 mL/min. The injection volume was set as 20 μL. The column temperature was 30 °C and the detector wavelength was 254 nm. Electron paramagnetic resonance (EPR) spectra were obtained on Bruker EMX plus X-band CW EPR spectrometer (microwave frequency, 9.83 GHz; microwave power, 2.00 mW). The degradation intermediates of ACV were identified by ultra-high performance liquid chromatography coupled with quadrupole time-of-flight mass spectrometry (UPLC-Q-TOF-MS, Agilent 1290 Infinity UHPLC System) with an electrospray ionization (AJS ESI) source operating in the positive scan mode. The determination of ROS and electrochemistry experiment were presented in Text S2-S7.

## 3. Results and discussion

### 3.1. Characterization

The dimensional morphology of Fe-SAC was observed through TEM. The TEM micrographs revealed that Fe-SAC was composed of wrinkled nanosheets, which was beneficial for exposing more active sites and enhancing catalytic efficiency. Meantime, the absence of metal clusters showed a homogeneous dispersion of metal atoms (Fig. 1a-b).

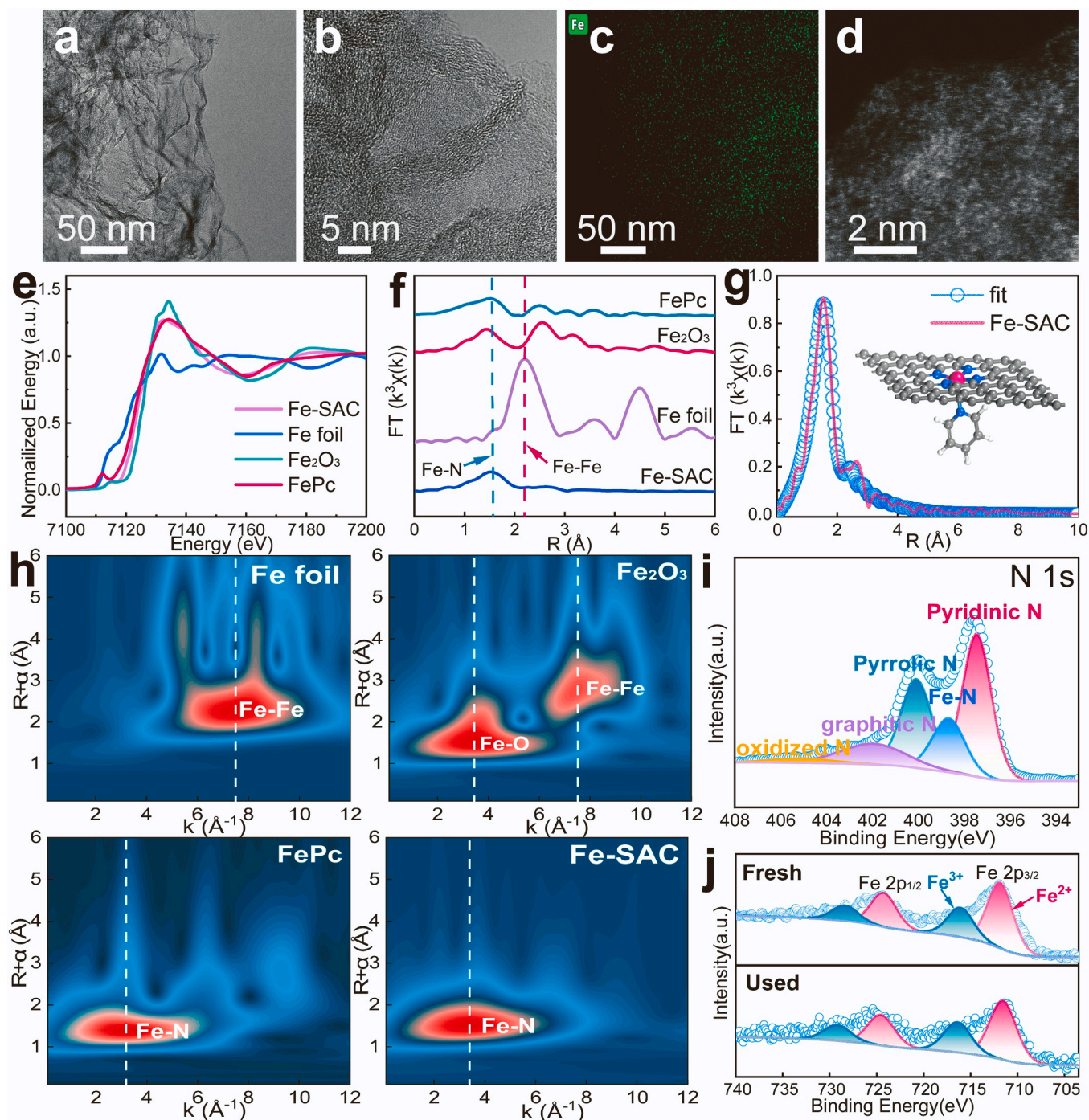


**Fig. 1.** (a–b) TEM images of Fe-SAC, (c) EDS mapping images of Fe, (d) AC-HAADF-STEM images of Fe-SAC, (e) Fe K-edge XANES spectra of Fe-SAC, Fe foil,  $\text{Fe}_2\text{O}_3$  and FePc, (f) FT  $k^3$ -weighted EXAFS spectra of Fe-SAC and reference samples, (g) corresponding EXAFS R-space fitting curve of the Fe-SAC sample, the inset is the corresponding  $\text{Fe-N}_5$  moiety, (h) WT of Fe-SAC in comparison with Fe foil,  $\text{Fe}_2\text{O}_3$ , and FePc, XPS spectra of Fe-SAC: (i) N 1s core level and (j) Fe 2p core level.

Furthermore, AC-HAADF-STEM was adopted to investigate the distribution of Fe species at the atomic level, the corresponding EDX mapping image of Fe indicated a uniform distribution of Fe atoms (Fig. 1c). As shown in Fig. 1d, the isolated bright spots corresponding to Fe atoms could be clearly distinguished because of the higher electron density relative to that of C and N atoms [23,36]. Subsequently, ICP-OES indicated that the actual load rate of Fe was 1.68 wt% for Fe-SAC (Table S1). From the findings mentioned above, Fe-SAC catalyst with a highly-dispersed single Fe atom was successfully prepared.

Furthermore, XAFS was implemented to probe into the metal coordination environment and undraped the presence of the Fe-N-C

configuration [50]. As displayed in Fig. 1e, the Fe K-edge X-ray absorption near-edge structure (XANES) spectrum indicated the absorption edge of Fe-SAC situated between  $\text{Fe}_2\text{O}_3$  and iron phthalocyanine (FePc), which forecasted that the valence state of the Fe atom in the Fe-SAC was between  $\text{Fe}^{2+}$  and  $\text{Fe}^{3+}$ . As shown in Fig. 1f, the Fourier transformed (FT)  $k^3$ -weighted EXAFS spectra of the Fe-SAC catalyst entirely revealed one major peak at 1.5 Å, which can be attributed to the first coordination shell of Fe-N. Meanwhile, Fe-SAC showed no peaks of Fe-Fe bond at 2.2 Å or 2.6 Å, compared with Fe foil and  $\text{Fe}_2\text{O}_3$ , which further indicated no clusters or crystalline particles were generated. EXAFS R-space fitting curve and EXAFS fitting parameters showed Fe



atom appeared in Fe-SAC fitted the scattering path of Fe-N<sub>5</sub>, and the corresponding Fe-N bond length was 2.02 Å (Fig. 1 g, Table S2). Moreover, wavelet transform (WT) analysis can distinguish the backscattering atoms, which are also operated for intuitional analysis [43]. As shown in Fig. 1 h, only a maximum intensity at  $\sim 3.2 \text{ Å}^{-1}$  was detected in Fe-SAC, demonstrating the signal of the Fe-N bond without the Fe-Fe signal. Based on the certification hereinabove, the metal of Fe-SAC was constructed from Fe-N<sub>5</sub> single atomic active center, which matched well with the results of AC-HAADF-STEM.

The XPS survey spectrum manifested the states of elements on the surface of as-prepared Fe-SAC (Fig. 1i-j). The spectrum of N 1s was deconvoluted into five peaks at 397.5, 398.7, 400.1, 401.9, and 404.9 eV, corresponding to pyridinic N, Fe-N, pyrrolic N, graphitic N, and oxidized N, respectively [23,36,51–53]. The primitive state of Fe was compared with the catalyst after five continuously catalytic reactions, four deconvoluted Fe 2p spectra in the Fe-SAC catalyst were ascribed to Fe<sup>2+</sup> 2p<sub>3/2</sub>, Fe<sup>3+</sup> 2p<sub>3/2</sub>, Fe<sup>2+</sup> 2p<sub>1/2</sub>, and Fe<sup>3+</sup> 2p<sub>1/2</sub>, respectively [17,23,54,55]. It can be seen that the XPS of Fe were untouched after the reaction, reflecting that if single Fe atom as an active center was not susceptible to interference during the recycling. The conclusion was consistent with performed excellent recyclability of Fe-SAC, and the

removal rate can be maintained at 98.0% after five cycles (Fig. S1).

### 3.2. Theoretical calculations and catalytic mechanisms

Firstly, the density functional theory (DFT) calculations were used to shed light on the adsorption energies and electron distribution to initially understand the discriminative mechanisms in different catalytic systems. Bader charge was calculated to investigate the charge distribution of Fe-SAC. As shown in Fig. 2a, the charge distribution 3D-image of the Fe-SAC intuitively indicated the electron density of Fe was significantly higher than that of the surrounding N, further proving that Fe atom might be the active site.

Additionally, Fe active site in the catalyst was positively charged and the electronegativity of the O atom of oxidants was minim which could cause strong coordination ability between them. As a result, the adsorption models were built by adsorption of O at different sites of the oxidant on the Fe-SAC, and the top view of the adsorption models of three systems were shown in Fig. S2-S4. The models' frontal views and corresponding adsorption energy ( $E_{\text{ads}}$ ) were shown in Fig. 2b. The optimal adsorption structure models of PMS, H<sub>2</sub>O<sub>2</sub>, and PDS corresponding  $E_{\text{ads}}$  were  $-2.659$ ,  $-0.618$ , and  $-4.226$  eV, respectively. The

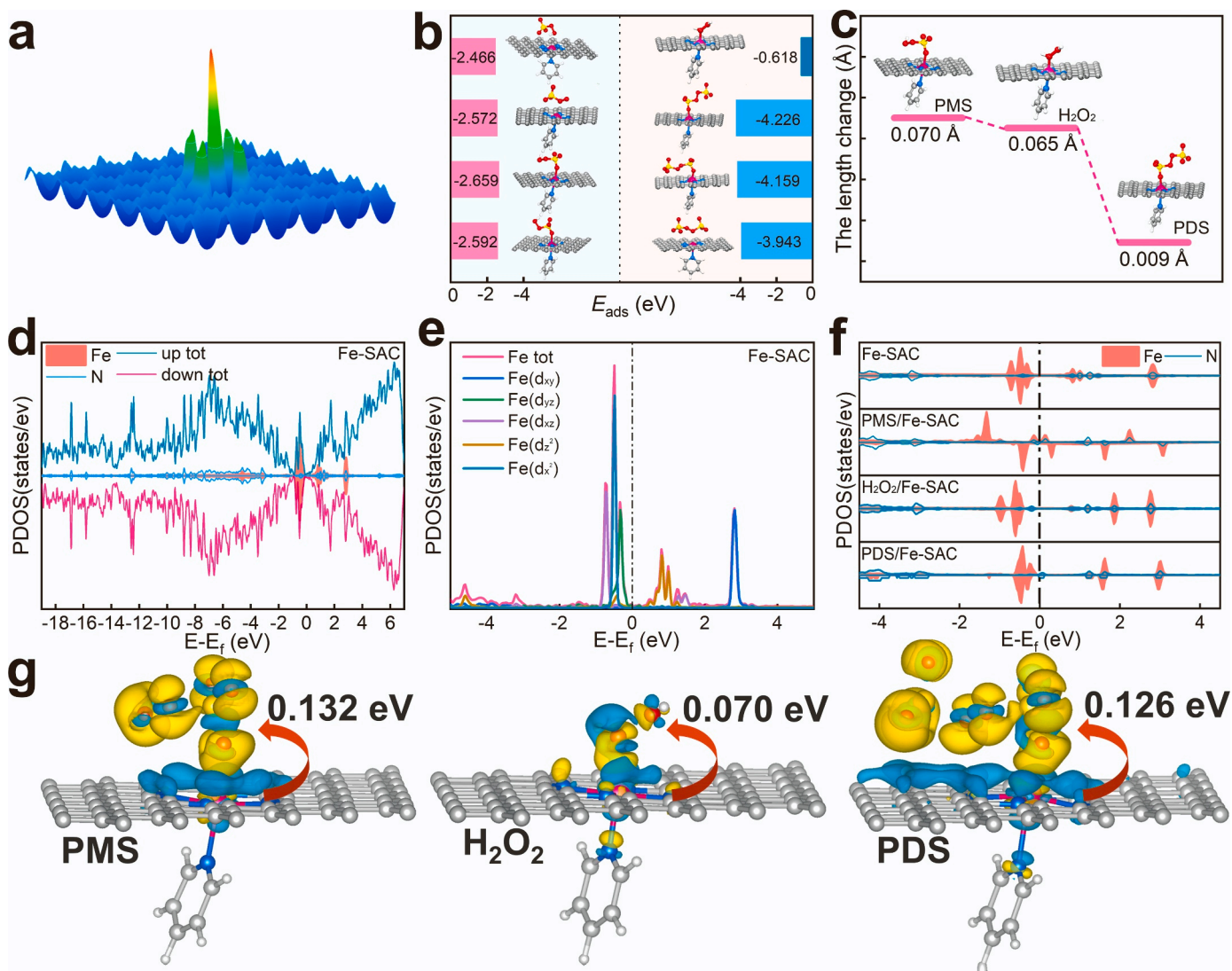


**Fig. 2.** (a) Charge distribution 3D-image for the Fe-SAC, (b) adsorption models and corresponding  $E_{\text{ads}}$  at different O sites of PMS (red), H<sub>2</sub>O<sub>2</sub> (green), PDS (blue) on Fe-SAC, respectively, (c) the length changes of O-O bond of PMS, PDS, and H<sub>2</sub>O<sub>2</sub> after adsorption on Fe-SAC, respectively, (d) PDOS of Fe-SAC, (e) PDOS of Fe 3d in Fe-SAC, (f) PDOS of Fe 3d and N 2p in different systems of Fe-SAC, (j) charge density difference in optimized configurations of PMS/Fe-SAC, H<sub>2</sub>O<sub>2</sub>/Fe-SAC, PDS/Fe-SAC by DFT calculation, respectively, electron transfer numbers were indicated on the configurations.

negative value of  $E_{\text{ads}}$  indicated spontaneous adsorption in each system. The weakest adsorption of  $\text{H}_2\text{O}_2$  on Fe-SAC was partly due to the Fe atom of the active site having a positive charge, meanwhile, PMS and PDS possessed a negative charge. As a result, Fe-SAC had stronger electrostatic attraction to PMS and PDS. Since all three oxidants have O-O bonds, the bond length changes of PMS,  $\text{H}_2\text{O}_2$ , and PDS were explored, which showed 0.070, 0.065, and 0.009 Å, respectively (Fig. 2c). The phenomenon indicated that Fe- $\text{N}_5$  active sites had the stronger activation effect on PMS,  $\text{H}_2\text{O}_2$ , and the weaker activation effect on PDS.

The density of states (DOS) can represent how electrons were distributed throughout different orbitals, as well as disclose essential details about chemical bonds and atom-to-atom interactions. The DOS diagram of Fe-SAC, as displayed in Fig. 2d, revealed that the orbits of Fe and N were the primary orbits close to the Fermi level, further confirming that Fe- $\text{N}_5$  was the active site of Fe-SAC. The projected density of state (PDOS) of the Fe 3d orbital revealed that  $d_{yz}$ ,  $d_{xz}$ , and  $d_x^2$  contributed primarily to the valence band, while  $d_{xy}$  and  $d_z^2$  contributed to the conduction band (Fig. 2e). Meanwhile,  $d_{yz}$  was the highest occupied orbital and  $d_z^2$  was the lowest unoccupied orbital. As displayed in Fig. 2f, the part density of states (PDOS) of Fe 3d had a large effect compared with the Fe-SAC after adsorption oxidants, and the PDOS of N 2p with a small effect indicated N didn't change after adsorption. Simultaneously, the PDOS analysis of Fe in the three catalytic systems revealed conduction band orbitals on the right side around Fermi all increased, indicating that the orbitals lost occupied electrons after adsorption. Furthermore, the PDOS of Fe increased the most near the Fermi level in the PDS/Fe-SAC system, and the electrons near the Fermi level were active. It indicated that the interaction force between Fe-SAC and O atom in this system was the strongest. The phenomenon was consistent with the calculation results of the value of the  $E_{\text{ads}}$ .

Charge density differences of the optimal configuration were calculated to study the change of electron distribution after adsorption (Fig. 2g). Significant electron transfer could be identified in the three systems, reflecting the chemisorption on the Fe- $\text{N}_5$  site. Furthermore, Bader charge calculations were performed to shed light on regulating the electronic structure of Fe active sites for activation. The electron

transfer value was 0.132, 0.070, and 0.126 eV of PMS,  $\text{H}_2\text{O}_2$ , and PDS, respectively, which was consistent with the results of earlier calculations that orbitals of Fe lost occupied electrons by PDOS analyses.

In summary, theoretical calculations indicated Fe- $\text{N}_5$  was the active site of Fe-SAC. PMS could be adsorbed effectively on the Fe-SAC, meantime the amount of electron transfer and the change of O-O bond length of PMS was the largest. For PDS, the adsorption capacity was the strongest and the amount of electron transfer was large. However, the effect on O-O bond was significantly weak. Compared with PMS, the predicted activation effect of PDS might be worse. Afterward, the adsorption energy of  $\text{H}_2\text{O}_2$  was weak and the number of electron transfer was small. But its activation effect on O-O bond was obvious, and the O-O bond could be disconnected to form the active substance  $^{\bullet}\text{OH}$ , which had strong oxidation capacity. Therefore, Fe-SAC was estimated to catalyze  $\text{H}_2\text{O}_2$  for degrading pollutants effectively.

### 3.3. Catalytic performance of Fe-SAC

To determine the catalytic capacity of Fe-SAC for different oxidants (PMS,  $\text{H}_2\text{O}_2$ , PDS), ACV was used as the target pollutant for the degradation experiments. It should be emphasized that the utilization rate of  $\text{H}_2\text{O}_2$  was low when it participated in AOPs [42]. Therefore, the concentration of  $\text{H}_2\text{O}_2$  was set at 10 mM in the following experiments. As shown in Fig. 3a, almost complete degradation of ACV can be performed in the PMS/Fe-SAC and  $\text{H}_2\text{O}_2$ /Fe-SAC systems within 10 min and 30 min, respectively. Moreover, the ACV removal efficiency of the PDS/Fe-SAC system was only 81.9% in 60 min of treatment, which was lower than those of PMS/Fe-SAC and  $\text{H}_2\text{O}_2$ /Fe-SAC systems. As displayed in Fig. 3b, the  $k_{\text{obs}}$  was positively correlated with the change of O-O bond length by DFT calculation. The O-O bond elongation of PMS was the largest, meantime degradation rate of pollutants was the most efficient. Therefore, mechanisms for peroxy activation via the Fe-SAC might be probably related to the change of O-O bond.

The concentrations of leached iron ions in PMS/Fe-SAC,  $\text{H}_2\text{O}_2$ /Fe-SAC, and PDS/Fe-SAC systems were 47.92, 82.38, and 47.97  $\mu\text{g/L}$  (Fig. 3c), respectively. As shown in Fig. S5, 100  $\mu\text{g/L}$   $\text{Fe}^{2+}$  had little

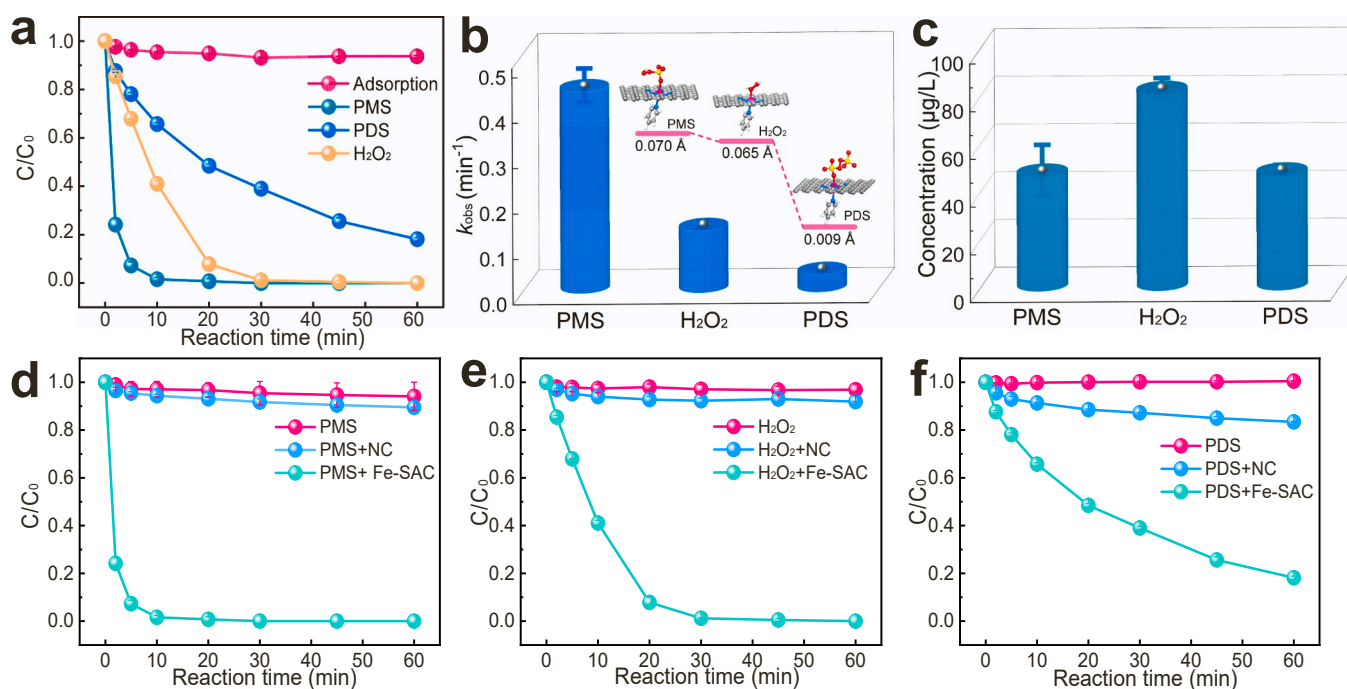


**Fig. 3.** (a) ACV removal efficiencies in different systems, (b) the  $k_{\text{obs}}$  in three systems and corresponding change of O-O by DFT calculation, (c) dissolution of Fe ions, (d-f) control experiments of various systems. (Experiment conditions: [pollutants]<sub>0</sub> = 2 mg/L, [catalyst]<sub>0</sub> = 150 mg/L, [PMS]<sub>0</sub> = 0.5 mM, [ $\text{H}_2\text{O}_2$ ]<sub>0</sub> = 10 mM, [PDS]<sub>0</sub> = 0.5 mM, T = 25 °C).

effect on ACV degradation by activating the oxidant alone, indicating the homogeneous catalysis of leaching iron ions could be ignored. Moreover, it can be seen from Fig. 3d-f that the degradation rates of ACV by sole oxidants were negligible. After adding N-doped carbon without Fe atoms (NC), the degradation rates were 10.5%, 8.0%, and 16.6%, respectively. However, they were significantly lower than the degradation rate of the oxidizer and Fe-SAC system, further indicating that Fe-N<sub>5</sub> was the active site of Fe-SAC.

### 3.4. Determination of ROS and unraveling the discriminative mechanisms

The main ROS were analyzed by quenching experiments, electron paramagnetic resonance (EPR) tests, and chemical probe experiments in PMS/Fe-SAC, H<sub>2</sub>O<sub>2</sub>/Fe-SAC, and PDS/Fe-SAC systems, respectively, details were shown in Text S2. And fitting lines and parameters of quenching experiments were shown in Fig. S6 and Table S3-5. The quenching experiment showed that TBA and FFA had an obvious inhibition effect compared with MeOH and *p*-BQ in the PMS/Fe-SAC system, indicating that there might have a certain amount of SO<sub>4</sub><sup>•−</sup>, <sup>•</sup>OH and <sup>1</sup>O<sub>2</sub> (Fig. 4a and b). *p*-BQ possibly reacted with PMS to form active complexes, that might promote the degradation of ACV [56,57]. Then with the increase of FFA input, the inhibition effect on ACV degradation became stronger, when FFA concentration was 50 mM, the degradation rate of pollutants decreased to 31.4% (Fig. S7). In the H<sub>2</sub>O<sub>2</sub>/Fe-SAC

system, the degradation of ACV was significantly inhibited with the addition of TBA or IPA (Fig. 4c and d). When the concentration of TBA was 10 mM, only 15.2% of ACV was degraded. Then 500 mM TBA completely inhibited the degradation of ACV, indicating that there was simply a certain amount of <sup>•</sup>OH. As shown in Figs. 4e and 4f, the corresponding *k*<sub>obs</sub> were 0.024, 0.034, 0.035, and 0.0007 min<sup>−1</sup> with the addition of *p*-BQ, MeOH, TBA, and FFA in PDS/Fe-SAC system, respectively. Therefore, *p*-BQ and FFA had obvious inhibition effects compared with MeOH and TBA, indicating that there might be a certain amount of O<sub>2</sub><sup>•−</sup> and <sup>1</sup>O<sub>2</sub>. Moreover, the potassium thiocyanate (KSCN) poison experiment reflected that the single Fe atoms were active sites of the three systems.

Besides, the EPR experiments were conducted to further explore the existence of ROS. As displayed in Fig. 4g, the strong 1:1:1 triplet signal for the characteristic peaks of <sup>1</sup>O<sub>2</sub> could only be detected in PMS/Fe-SAC system. As shown in Fig. S8a, the peak intensity increased obviously in PMS/Fe-SAC system compared with sole PMS and NC/PMS systems. Moreover, the peak intensity increased gradually, indicating that more singlet oxygen was generated with the extension of time (Fig. S8b). Chemical probe experiments were conducted to further explore the existence of <sup>1</sup>O<sub>2</sub> in PMS/Fe-SAC system. As displayed in Fig. S9, the deionized water was replaced with pure methanol solution in the PMS/Fe-SAC system to increase the solubility of  $\beta$ -carotene (quenching agent of <sup>1</sup>O<sub>2</sub>). The degradation rate decreased from 100% to 33.4% observably

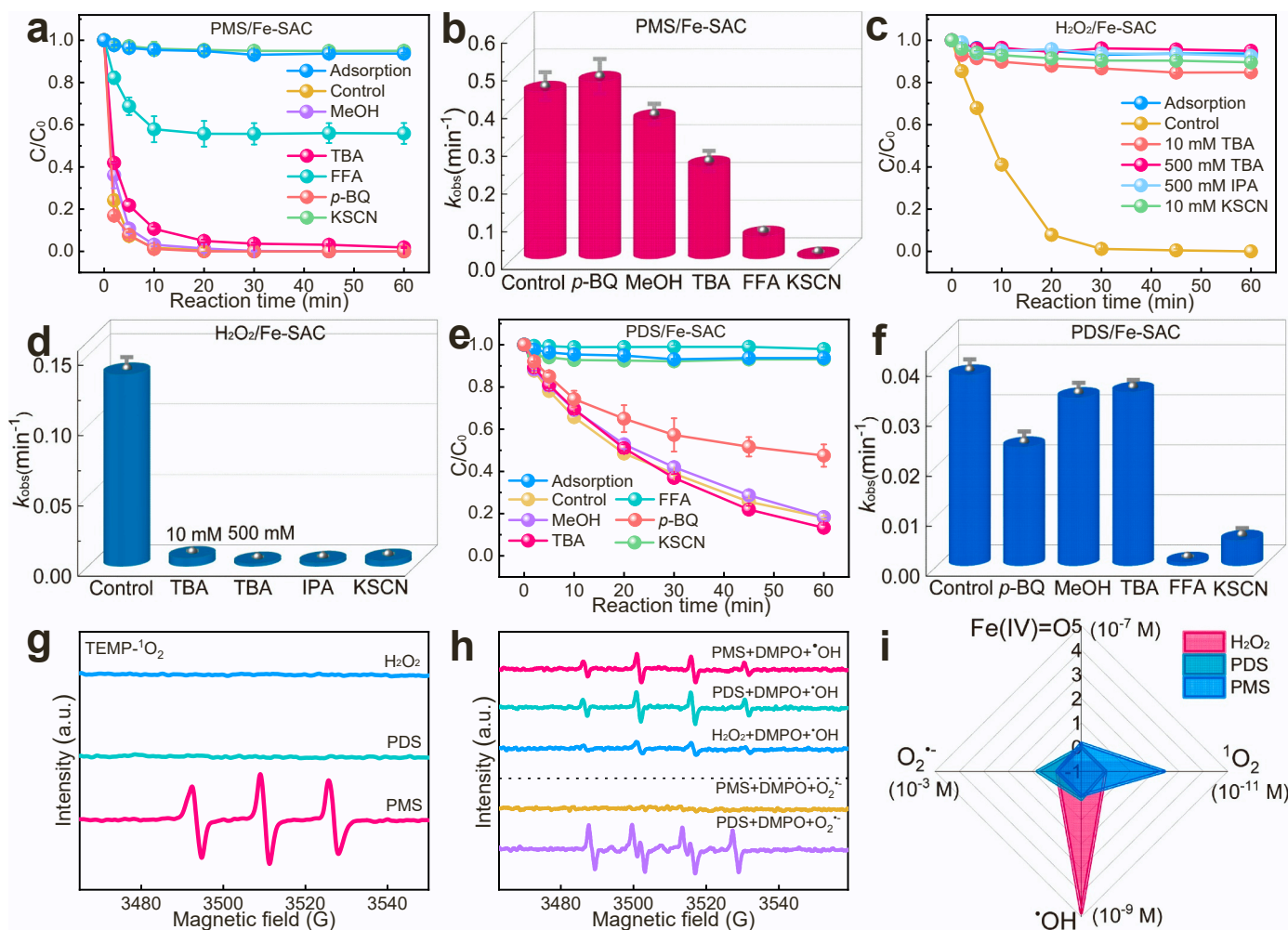
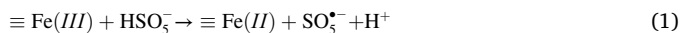


**Fig. 4.** (a-c) The effects of different scavengers on ACV degradation in PMS/Fe-SAC, H<sub>2</sub>O<sub>2</sub>/Fe-SAC, and PDS/Fe-SAC systems, respectively, (d-f) correspondingly variation of *k*<sub>obs</sub> by different scavengers, (g) TEMP-trapped EPR spectra of different systems, (h) EPR spectra of different systems with DMPO as the trapping agent, (i) the concentrations of active substances in the three AOPs system. (Experimental conditions: TBA = 500 mM, MeOH = 500 mM, FFA = 20 mM, *p*-BQ = 5 mM, KSCN = 10 mM).

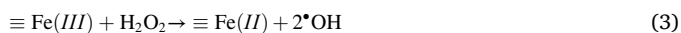


upon the addition of  $\beta$ -carotene, indicating that PMS/Fe-SAC was a  $^1\text{O}_2$ -dominated system. Moreover, three possible pathways were proposed to clarify the formation of  $^1\text{O}_2$  in PMS/Fe-SAC system [58]: (a) PMS generated  $\text{SO}_5^{\bullet-}$ , which then self-react to form  $^1\text{O}_2$ ; (b)  $\text{O}_2^{\bullet-}$  produced by the conversion of dissolved oxygen or PMS reacting with  $\text{H}_2\text{O}$  can convert to  $^1\text{O}_2$  indirectly; (c) self-decomposition of PMS. When aniline was added as a scavenger for  $\text{SO}_5^{\bullet-}$  in the system, the degradation of ACV was inhibited, however, aerating  $\text{N}_2$  had almost no inhibition effect (Fig. S10). Due to the self-decomposition of the PMS process being negligible,  $^1\text{O}_2$  was mainly generated by the self-reaction of  $\text{SO}_5^{\bullet-}$  (Eq. (1) and eq. (2)).

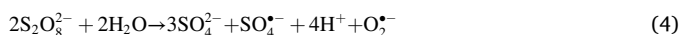


Furthermore, the EPR experiment was contradicted by the quenching experiment of  $^1\text{O}_2$  in PDS/Fe-SAC system. Accordingly,  $^1\text{O}_2$  fluorescent probe experiment was conducted by Singlet Oxygen Sensor Green (SOSG) fluorescence probe to further determine  $^1\text{O}_2$  (Text S3). In the standard control system, an obvious fluorescence absorption peak can be detected after adding  $\text{NaClO}$  within 1 min. However, there was no corresponding fluorescence absorption peak was detected in PDS/Fe-SAC system, which indicated the absence of  $^1\text{O}_2$  (Fig. S11). The inhibition of degradation rates of ACV by FFA might be ascribed to the passivation effect on the surface of Fe-SAC [18,59].

Additionally, the EPR displayed the characteristic quartet for  $\text{DMPO} \cdot \text{OH}$  adducts with intensity ratios of 1:2:2:1 in three systems [60], but strong  $\text{DMPO} \cdot \text{O}_2^{\bullet-}$  adduct just detected in PDS/Fe-SAC system (Fig. 4 h). Combined with the quenching experiment, there was only a certain amount of  $\cdot\text{OH}$  in the  $\text{H}_2\text{O}_2/\text{Fe-SAC}$  system, and the formation mechanism was shown in Eq. (3).



Meantime, a certain amount of  $\cdot\text{OH}$  existed in all three systems and  $\text{O}_2^{\bullet-}$  only presented in PDS/Fe-SAC system. To clarify the role of  $\text{O}_2^{\bullet-}$  in different catalytic systems, NBT was added to a solution containing  $\text{O}_2^{\bullet-}$ . Formazan could be formed and the solution assumed a purple hue if  $\text{O}_2^{\bullet-}$  existed. Furthermore, NBT was not consumed as the probe in PMS/Fe-SAC system (Fig. S12), which further indicated the absence of  $\text{O}_2^{\bullet-}$ . It can be seen in Fig. S13a that when only PDS existed, the concentration of NBT did not change significantly with temporal evolution. Meantime, NBT was consumed and even when the initial concentration of NBT increased to 0.5 mM, the absorbance value of NBT sharply dropped after just 30 s (Fig. S13b-c). Owing to the addition of Fe-SAC would affect the absorbance value of NBT, the sample must be filtered with 0.22  $\mu\text{m}$  PTFE syringe filter discs before the UV scan. Therefore, monoformazan (MF) and diformazan (DF) were filtered out because of their insolubility, so there was no corresponding fluorescence absorption peak of MF or DF. However, it can be observed that the light yellow NBT solution gradually turned blue and formed a bluish-white flocculent MF, indicating the existence of  $\text{O}_2^{\bullet-}$  in the PDS/Fe-SAC system (Fig. S14). Afterward, no obvious change was observed in ACV degradation after  $\text{N}_2$  bubbling shown in Fig. S15, suggesting that dissolved oxygen plays a negligible role in the generation of  $\text{O}_2^{\bullet-}$ . The deionized water was replaced with pure methanol solution in the PDS/Fe-SAC system to identify whether the evolution of  $\text{O}_2^{\bullet-}$  was related to the  $\text{H}_2\text{O}$  in the system (Fig. S16). Methanol significantly inhibited the degradation of ACV, which indicated the formation of  $\text{O}_2^{\bullet-}$  which may be due to the hydrolysis of PDS (Eq. (4) and eq. (5)) [61].



To explore other nonradical pathways, methyl phenyl sulfoxide (PMSO) as a probe compound can react with high-valent iron-oxo and

the generation of methyl phenyl sulfone ( $\text{PMSO}_2$ ) close to 100% [62,63]. In PMS/Fe-SAC system, FFA and  $\beta$ -carotene cannot inhibit completely, suggesting that there were other nonradical pathways potentially. Therefore, as shown in Fig. S17, the initial concentrations of PMSO were 10, 20, and 50  $\mu\text{M}$ , respectively, with the decrease of the initial concentrations, the degradation rate of PMSO increased gradually. But the conversion rate was always close to 100%, indicating the existence of high-valent iron-oxo species ( $\text{Fe(IV)=O}$ ). However, in  $\text{H}_2\text{O}_2/\text{Fe-SAC}$  system, no obvious signal of  $\text{PMSO}_2$  was detected, indicating the absence of high-valent iron-oxo species (Fig. S18), and the degradation of PMSO was due to the decomposition of  $\cdot\text{OH}$ . Meantime, in PDS/Fe-SAC system, just 5.1% of the PMSO was consumed, but the conversion rate was not 100% (Fig. S19). The consumption of PMSO may be due to its self-decomposition and the formation of  $\text{PMSO}_2$  was likely due to the role of  $\text{O}_2^{\bullet-}$  [64]. Therefore  $\text{Fe(IV)=O}$  was only involved in PMS/Fe-SAC system.

In order to further quantify the content of active substances in the three systems, FFA, coumarin, PMSO, and NBT were used as probes to quantify  $^1\text{O}_2$ ,  $\cdot\text{OH}$ ,  $\text{Fe(IV)=O}$ , and  $\text{O}_2^{\bullet-}$ , respectively. In conclusion, by comparing the three different reaction systems, it can be seen that the three systems all contained  $\cdot\text{OH}$ , but the PMS/Fe-SAC system also contained  $^1\text{O}_2$  and  $\text{Fe(IV)=O}$ , and  $\text{O}_2^{\bullet-}$  was involved in PDS/Fe-SAC system. As shown in Fig. 4i, in PMS/Fe-SAC system, the steady-state concentrations of  $\cdot\text{OH}$ ,  $^1\text{O}_2$ , and  $\text{Fe(IV)=O}$  were calculated to be 0.0014 nmol/L, 0.024 nmol/L, and 0.015  $\mu\text{M}$ , respectively (Fig. S20-21, Test S4-5). And the steady-state concentration of  $\cdot\text{OH}$  was calculated to be 4.83 nmol/L in the  $\text{H}_2\text{O}_2/\text{Fe-SAC}$  system (Fig. S22). Afterward, in PDS/Fe-SAC system, the steady-state concentrations of  $\text{O}_2^{\bullet-}$  and  $\cdot\text{OH}$  were calculated to be 0.793 mmol/L and 0.157 nmol/L, respectively (Fig. S23-24, Text S6).

Finally, the premixing experiments and electrochemical measurement (Text S7) were conducted to verify the existence of a direct electron transfer path in the system. As shown in Fig. S25a-c, the results of premixing experiments implied that the degradation effect became worse with the prolongation of premixing time, which indicated the existence of free radical pathway in three systems. The chronoamperometry was conducted to explore the voltage variation of the system. According to the open circuit potential diagram of the PMS/Fe-SAC system (Fig. 5a), the reductive oxidation potential of the oxidant can be significantly increased with the Fe-SAC. After the addition of ACV, the potential of the PMS/ACV system had no change, indicating that the PMS alone didn't react with ACV. While the potential of the PMS/Fe-SAC/ACV system slightly decreased, indicating a direct electron transfer path might exist or the formation of  $\text{Fe(IV)=O}$ . Then Fig. 5b showed the open circuit potential diagram in PDS/Fe-SAC system, the presence or absence of Fe-SAC had no significant effect on the increase of reductive oxidation potential after the addition of PDS. After the addition of pollutants, the potential of systems had no change, further indicating the absence of a high-value metal transition intermediate and no electron transfer in the PDS/Fe-SAC system.

To further research, a salt bridge experiment was conducted as shown in Fig. 5c, the two half cells were connected by an agar salt bridge to maintain electrical neutrality during the reaction. According to the consequences of the salt-bridge experiment, when PMS was added to PMS/Fe-SAC system, the current increased sharply up to 83.1  $\mu\text{A}$  and then decreased gradually over time (Fig. 5d). Interestingly, the change of current was consistent with the trend of PMS concentration. Based on previous research, the obvious electric current in PMS/Fe-SAC system might be from the formation of  $\text{Fe(IV)=O}$  transition intermediate. Meantime, when PDS was added to PDS/Fe-SAC system, the current increased merely up to 15.9  $\mu\text{A}$ , remained unchanged basically over time, and the concentration of PDS changed mildly (Fig. 5e). However, as shown in Fig. 5f, the pollutants couldn't be degraded even after 48 h in both systems. Above all, there was no direct electron transfer path in PMS/Fe-SAC and PDS/Fe-SAC systems.

Afterward, the degradation intermediates of ACV in three diverse systems were detected by UPLC-Q-TOF-MS shown in Fig. S26-28,

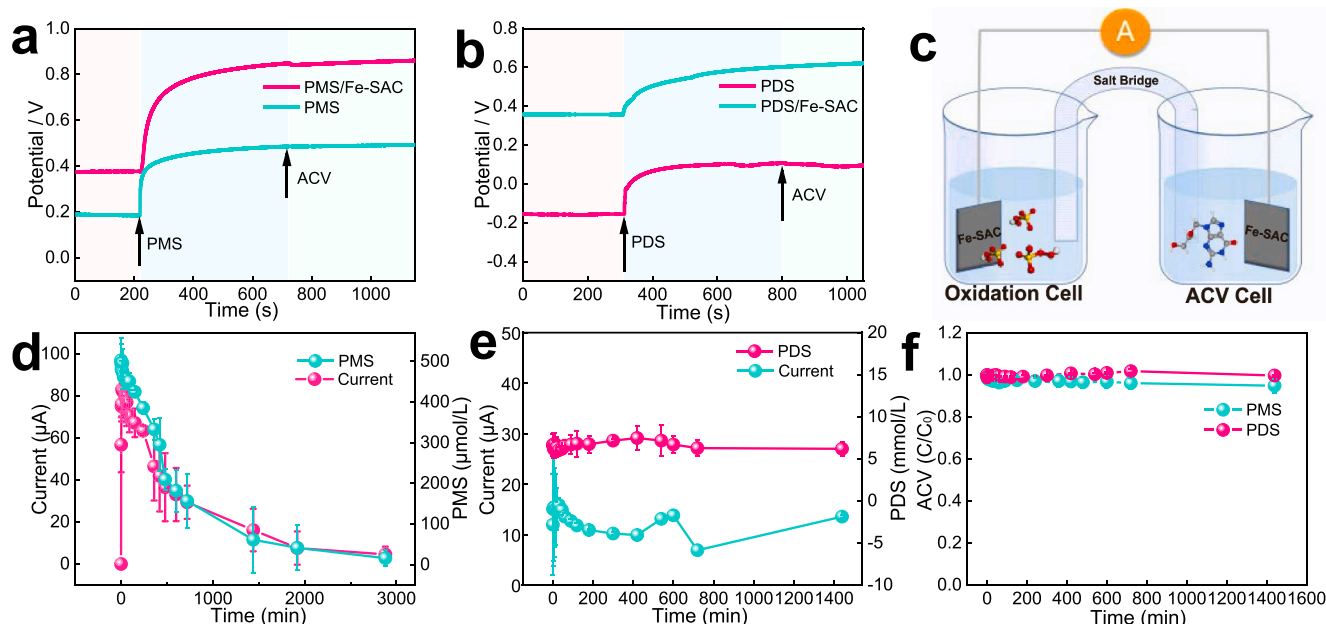


**Fig. 5.** (a) The chronoamperometry curves of PMS/Fe-SAC system in 0.05 M Na<sub>2</sub>SO<sub>4</sub> electrolyte solution, (b) the chronoamperometry curves of PDS/Fe-SAC system in 0.05 M Na<sub>2</sub>SO<sub>4</sub> electrolyte solution, (c) schematic diagram of the salt bridge experiment, (d) the variation of current magnitude, and oxidant consumption during the reaction in PMS/Fe-SAC system, (e) the variation of current magnitude and oxidant consumption during the reaction in PDS/Fe-SAC system, (f) the variation of pollutant degradation of salt bridge experiment.

respectively [65–67]. As shown in Fig. S29, the degradation pathways were speculated, ACV ( $m/z$  226.0910) radical attacking was able to open the six-member heterocycle to form  $m/z$  214 or 230 in three systems. Then dehydroxylation process occurred on the long side chain of intermediate product  $m/z$  230, and form  $m/z$  214. The hydroxyl group that's taken off was likely to combine with H to form H<sub>2</sub>O molecules. Specially, the amino group of ACV six-membered ring underwent elimination reaction, and two H atoms were removed to form  $m/z$  238 in PDS/Fe-SAC system. In addition, the branch chain of ACV could be broken directly by oxidation of the C-C bond and the final product was  $m/z$  152. Eventually,  $m/z$  214 would degrade to form H<sub>2</sub>O, CO<sub>2</sub>, and NH<sub>4</sub><sup>+</sup>.

### 3.5. Practical application potential of Fe-SAC

A majority of studies on single-atom materials remain in the laboratory dimension due to the circumstance. However, actual water bodies possess miscellaneous types and complex compositions. Certain anionic and organic compounds are likely to impact the degradation of target pollutants by the catalyst [20,68,69]. Proposed in this regard, the resistance of Fe-SAC to different anions (Cl<sup>−</sup>, HCO<sub>3</sub><sup>−</sup>, H<sub>2</sub>PO<sub>4</sub><sup>−</sup>), organic matter (HA), and the application effect in actual water (tap water, lake water, and river water) were explored.

In PMS/Fe-SAC system, various coexisting substances (Cl<sup>−</sup>, HCO<sub>3</sub><sup>−</sup>, H<sub>2</sub>PO<sub>4</sub><sup>−</sup> and HA) have negligible influence on the degradation of target pollutants, and also showed impressive removal efficiencies in actual bodies (Fig. 6a–b). Because the system was a non-free radical-dominated system, it had a strong anti-interference ability. Accordingly, it indicated the splendid interference immunity of the PMS/Fe-SAC system against the actual water matrix conditions. For H<sub>2</sub>O<sub>2</sub>/Fe-SAC system (Fig. 6c–d), Cl<sup>−</sup> reacted with <sup>•</sup>OH to form ClOH<sup>•</sup> and ClOH<sup>•</sup> further reacted with H<sup>+</sup> to form Cl<sup>•</sup> under acidic conditions [70]. Because  $E^0(\text{Cl}^\bullet/\text{Cl}^-) = 2.5 \text{ V}_{\text{NHE}} > E^0(\text{OH}/\text{OH}^\bullet) = 1.9\text{--}2.7 \text{ V}_{\text{NHE}}$ , Cl<sup>−</sup> had a certain acceleration effect on the degradation of ACV in the beginning [6]. The addition of HCO<sub>3</sub><sup>−</sup> or H<sub>2</sub>PO<sub>4</sub><sup>−</sup> inhibited the degradation of target pollutants, since the presence of buffer ions would affect the pH of the reaction system, and thus affected the activation effect of H<sub>2</sub>O<sub>2</sub>. At the same time, the system only

contained <sup>•</sup>OH, HA would react with <sup>•</sup>OH competing with the target pollutant, which reduced the degradation effect. Moreover, the degradation rates of ACV were 90.0%, 22.9%, and 54.1%, respectively, in three actual bodies (tap water, lake water, and river water). The lake water had the strongest deterrent, presumably due to the high level of organic matter.

In addition, in PDS/Fe-SAC system (Fig. 6e–f), Cl<sup>−</sup> can promote the degradation of pollutants, and the degradation rate increased from 81.9% to 94.0%, which may also be due to the reaction with <sup>•</sup>OH to form Cl<sup>•</sup>. The ACV degradation efficiency declined to 48.7%, and 70.9% corresponding with the addition of HCO<sub>3</sub><sup>−</sup> and H<sub>2</sub>PO<sub>4</sub><sup>−</sup>. Because HCO<sub>3</sub><sup>−</sup> and H<sub>2</sub>PO<sub>4</sub><sup>−</sup> can consume <sup>•</sup>OH, afterward PDS could react with HCO<sub>3</sub><sup>−</sup> leading to the decreased utilization efficiency of PDS and further lowered ACV degradation efficiency [19,20]. The addition of HA-inhabited ACV degradation was due to radicals or oxidants depletion [71]. In three actual bodies (tap water, lake water, and river water), the degradation rates of ACV were 78.2%, 50.9%, and 66.1%, respectively. Lake water had the strongest inhibitory effect due to its' more complex with organic matter and ions.

To investigate the feasibility and performance of Fe-SAC used in continuous flow experiments were studied. Because PMS/Fe-SAC system had the most efficient degradation effect, PMS was chosen as the oxidant. A continuous flow device was set up as shown in Fig. 6g. The mixed solution of pollutants and PMS flowed through a filling column filled with Fe-SAC (120 mg), and the flow rate of the reaction solution was controlled by the peristaltic pump (2 mL/min). The effluent was collected at a certain interval and the concentration of pollutants was measured (Fig. 6h). A comparative study has shown that ACV could effectively degrade only when a catalyst and oxidant exist at the same time. The degradation rate of ACV remained near 100% in the first 160 h. The result indicated that the Fe-SAC could operate steadily for nearly 7 d with a daily processing capacity of 2640 mL ACV (2 mg/L).

## 4. Conclusion

In summary, Fe-SAC with FeN<sub>5</sub> catalytic sites can activate O-O bands of PMS (<sup>•</sup>OH, <sup>1</sup>O<sub>2</sub>, Fe(IV)=O), H<sub>2</sub>O<sub>2</sub> (<sup>•</sup>OH), and PDS (<sup>•</sup>OH, O<sub>2</sub><sup>•</sup>)



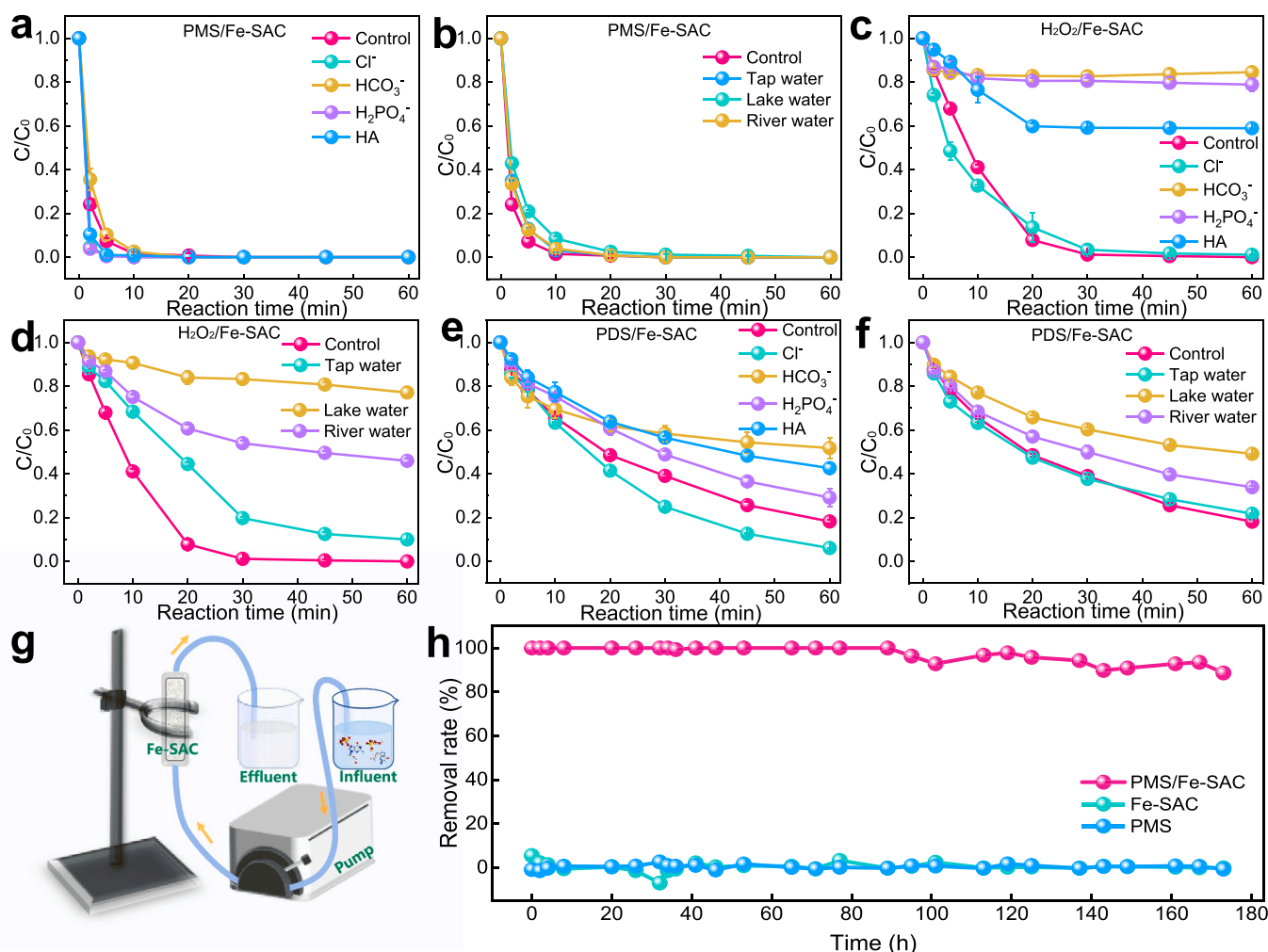


**Fig. 6.** (a-c) The effect of various coexisting substances on the ACV removal, (d-f) removal of ACV in actual water, (g) diagram of circulating flow experimental apparatus, (h) water purification effects in fixed bed reactor. (Experiment conditions:  $[pollutants]_0 = 2$  mg/L,  $[catalyst]_0 = 150$  mg/L,  $[PMS]_0 = 0.5$  mM,  $[H_2O_2]_0 = 10$  mM,  $[PDS]_0 = 0.5$  mM,  $T = 25$  °C,  $[Cl^-] = [HCO_3^-] = [H_2PO_4^-] = 5$  mM,  $[HA] = 10$  mg/L,  $T = 25$  °C, flow rate = 2 mL/min, the samples of tap water were collected from Sichuan University, lake water, and river water were taken from Fuhe River (104° 5'1", 30° 37'19") and Donghu Park (104° 5'2", 30° 37'15") in Chengdu, respectively).

efficiently, that produce diverse main active substances by the discriminative mechanisms. DFT calculation showed that Fe-SAC had the strongest adsorption capacity for PDS, while the influence on O-O bond was weak. Therefore, after the activation of PDS, the active substances and degradation products were likely to be difficult to desorption, and the degradation rate of ACV was affected in PDS/Fe-SAC system. Besides, the degradation effects of PMS/Fe-SAC and  $H_2O_2$ /Fe-SAC systems were better because of the suitable adsorption energy and stronger effect on the O-O bond. Moreover, the effect of inorganic anions and actual water enlightened that the corresponding oxidant could be selected to achieve the best treatment effect according to the conditions of water bodies. This study unveils the mechanism of activating different oxidants in a Fenton-like reaction by Fe-SAC. Excellent catalytic properties and prominent recyclability made Fe-SAC exploitable.

#### CRediT authorship contribution statement

**Xinyu Song:** Conceptualization, Formal analysis, Investigation, Writing – original draft, Writing – review & editing. **Yang Shi:** Supervision, Methodology, Formal analysis. **Zelin Wu:** Investigation, Formal analysis. **Bingkun Huang:** Formal analysis. **Xinhao Wang:** Formal analysis. **Heng Zhang:** Methodology. **Peng Zhou:** Methodology, Formal analysis. **Wen Liu:** Resources. **Zhicheng Pan:** Resources. **Zhaokun**

**Xiong:** Conceptualization, Data curation, Writing – review & editing, Project administration. **Bo Lai:** Validation, Conceptualization, Funding acquisition.

#### Declaration of Competing Interest

The authors declare that they have no known competing financial interests or personal relationships that could have appeared to influence the work reported in this paper.

#### Data availability

Data will be made available on request.

#### Acknowledgments

The authors would like to acknowledge the financial support from the National Key Research and Development Program of China (Grant No. 2021YFA1202500), the National Natural Science Foundation of China (No. 52200105), Sichuan Program of Science and Technology (2023NSFC0344, 2023JDZH0010, 2021ZDZX0012) and China Post-doctoral Science Foundation (2022M710993). The authors also would like to thank the Analytical & Testing Center of Sichuan University for

EPR detection.

## Appendix A. Supporting information

Supplementary data associated with this article can be found in the online version at doi:10.1016/j.apcatb.2023.123240.

## References

- [1] L. Yang, Z. Xiong, J. Li, Z. Wu, X. Zhao, C. Zhao, Y. Zhou, Y. Qian, B. Lai, Iron active sites encapsulated in N-doped graphite for efficiently selective degradation of emerging contaminants via peroxymonosulfate (PMS) activation: Inherent roles of adsorption and electron-transfer dominated nonradical mechanisms, *Chem. Eng. J.* 444 (2022), 136623.
- [2] C. Ling, X. Liu, H. Li, X. Wang, H. Gu, K. Wei, M. Li, Y. Shi, H. Ben, G. Zhan, C. Liang, W. Shen, Y. Li, J. Zhao, L. Zhang, Atomic-Layered Cu<sub>5</sub> Nanoclusters on FeS<sub>2</sub> with Dual Catalytic Sites for Efficient and Selective H<sub>2</sub>O<sub>2</sub> Activation, *Angew. Chem. Int. Ed. Engl.* 61 (2022), e202200670.
- [3] Y. Liu, Y. Zhao, J. Wang, Fenton/Fenton-like processes with in-situ production of hydrogen peroxide/hydroxyl radical for degradation of emerging contaminants: Advances and prospects, *J. Hazard. Mater.* 404 (2021), 124191.
- [4] Y. Yu, Z. Xiong, B. Huang, X. Wang, Y. Du, C. He, Y. Liu, G. Yao, B. Lai, Synchronous removal of pharmaceutical contaminants and inactivation of pathogenic microorganisms in real hospital wastewater by electro-peroxone process, *Environ. Int.* 168 (2022), 107453.
- [5] Y. Zou, J. Hu, B. Li, L. Lin, Y. Li, F. Liu, X. Li, Tailoring the coordination environment of cobalt in a single-atom catalyst through phosphorus doping for enhanced activation of peroxymonosulfate and thus efficient degradation of sulfadiazine, *Appl. Catal. B: Environ.* 312 (2022), 121408.
- [6] J. Lee, U.V. Gunten, J.H. Kim, Persulfate-based advanced oxidation: critical assessment of opportunities and roadblocks, *Environ. Sci. Technol.* 54 (2020) 3064–3081.
- [7] J. Wang, S. Wang, Reactive species in advanced oxidation processes: Formation, identification and reaction mechanism, *Chem. Eng. J.* 401 (2020), 126158.
- [8] J. Flanagan, W.P. Griffith, A.C. Skapski, The active principle of Caro's acid, HSO<sub>5</sub>: X-ray crystal structure of KHSO<sub>5</sub>·H<sub>2</sub>O, *Chem. Commun.* 23 (1984) 1574–1575.
- [9] W.-D. Oh, Z. Dong, T.-T. Lim, Generation of sulfate radical through heterogeneous catalysis for organic contaminants removal: Current development, challenges and prospects, *Appl. Catal. B: Environ.* 194 (2016) 169–201.
- [10] X. Duan, H. Sun, J. Kang, Y. Wang, S. Indrawirawan, S. Wang, Insights into heterogeneous catalysis of persulfate activation on dimensional-structured nanocarbons, *ACS Catal.* 5 (2015) 4629–4636.
- [11] I.M. Kolthoff, I.K. Miller, The Chemistry of Persulfate. I. The kinetics and mechanism of the decomposition of the persulfate ion in aqueous medium 1, *J. Am. Chem. Soc.* 73 (1951) 3055–3059.
- [12] I.A. Ike, K.G. Linden, J.D. Orbell, M. Duke, Critical review of the science and sustainability of persulfate advanced oxidation processes, *Chem. Eng. J.* 338 (2018) 651–669.
- [13] S. Wacławek, H.V. Lutze, K. Grübel, V.V.T. Padil, M. Černík, D.D. Dionysiou, Chemistry of persulfates in water and wastewater treatment: a review, *Chem. Eng. J.* 330 (2017) 44–62.
- [14] Y. Yu, C. Yu, Z. Wu, B. Huang, P. Zhou, H. Zhang, W. Liu, Y. Liu, Z. Xiong, B. Lai, Switching the primary mechanism from a radical to a nonradical pathway in electrocatalytic ozonation by onsite alternating anode and cathode, *Chem. Eng. J.* 457 (2023), 141340.
- [15] M. Yang, Z. Hou, X. Zhang, B. Gao, Y. Li, Y. Shang, Q. Yue, X. Duan, X. Xu, Unveiling the origins of selective oxidation in single-atom catalysis via Co-N<sub>4</sub>-C intensified radical and nonradical pathways, *Environ. Sci. Technol.* 56 (2022) 11635–11645.
- [16] K. Qian, H. Chen, W. Li, Z. Ao, Y.N. Wu, X. Guan, Single-Atom Fe Catalyst Outperforms Its Homogeneous Counterpart for Activating Peroxymonosulfate to Achieve Effective Degradation of Organic Contaminants, *Environ. Sci. Technol.* 55 (2021) 7034–7043.
- [17] X. Li, Y. Jia, M. Zhou, X. Su, J. Sun, High-efficiency degradation of organic pollutants with Fe, N co-doped biochar catalysts via persulfate activation, *J. Hazard. Mater.* 397 (2020), 122764.
- [18] F. Li, Z. Lu, T. Li, P. Zhang, C. Hu, Origin of the Excellent Activity and Selectivity of a Single-Atom Copper Catalyst with Unsaturated Cu-N<sub>2</sub> Sites via Peroxydisulfate Activation: Cu(III) as a Dominant Oxidizing Species, *Environ. Sci. Technol.* 56 (2022) 8765–8775.
- [19] M.M. Wang, L.J. Liu, J.T. Wen, Y. Ding, J.R. Xi, J.C. Li, F.Z. Lu, W.K. Wang, J. Xu, Multimetallic CuCoNi oxide nanowires in situ grown on a nickel foam substrate catalyze persulfate activation via mediating electron transfer, *Environ. Sci. Technol.* 56 (2022) 12613–12624.
- [20] X. Liu, Y. Liu, H. Qin, Z. Ye, X. Wei, W. Miao, D. Yang, S. Mao, Selective removal of phenolic compounds by peroxydisulfate activation: inherent role of hydrophobicity and interface ROS, *Environ. Sci. Technol.* 56 (2022) 2665–2676.
- [21] C. Ling, X. Liu, M. Li, X. Wang, Y. Shi, J. Qi, J. Zhao, L. Zhang, Sulphur vacancy derived anaerobic hydroxyl radical generation at the pyrite-water interface: Pollutants removal and pyrite self-oxidation behavior, *Appl. Catal. B: Environ.* 290 (2021), 120051.
- [22] Q. Wu, J. Wang, Z. Wang, Y. Xu, Z. Xing, X. Zhang, Y. Guan, G. Liao, X. Li, High-loaded single Cu atoms decorated on N-doped graphene for boosting Fenton-like catalysis under neutral pH, *J. Mater. Chem. A* 8 (2020) 13685–13693.
- [23] L. Chen, K. Xing, Q. Shentu, Y. Huang, W. Lv, Y. Yao, Well-dispersed iron and nitrogen co-doped hollow carbon microsphere anchoring by g-C<sub>3</sub>N<sub>4</sub> for efficient peroxymonosulfate activation, *Chemosphere* 280 (2021), 130911.
- [24] M. Cohen, N. Ferroudi, A. Combes, V. Pichon, S. Abramson, Tracking the degradation pathway of three model aqueous pollutants in a heterogeneous Fenton process, *J. Environ. Chem. Eng.* 7 (2019), 102987.
- [25] B. Huang, Z. Wu, H. Zhou, J. Li, C. Zhou, Z. Xiong, Z. Pan, G. Yao, B. Lai, Recent advances in single-atom catalysts for advanced oxidation processes in water purification, *J. Hazard. Mater.* 412 (2021), 125253.
- [26] M. Qian, X.L. Wu, M. Lu, L. Huang, W. Li, H. Lin, J. Chen, S. Wang, X. Duan, Modulation of charge trapping by island-like single-atom cobalt catalyst for enhanced photo-Fenton-like reaction, *Adv. Funct. Mater.* 33 (2023), 2208688.
- [27] S. Liu, Y. Hu, H. Xu, Z. Lou, J. Chen, C.Z. Yuan, X. Lv, X. Duan, S. Wang, X.-L. Wu, Directional electron transfer in single-atom cobalt enzyme for enhanced photo-Fenton-like reaction, *Appl. Catal. B: Environ.* 335 (2023), 122882.
- [28] X.L. Wu, S. Liu, Y. Li, M. Yan, H. Lin, J. Chen, S. Liu, S. Wang, X. Duan, Directional and Ultrafast Charge Transfer in Oxygen-Vacancy-Rich ZnO@Single-Atom Cobalt Core-Shell Junction for Photo-Fenton-Like Reaction, *Angew. Chem. Int. Ed. Engl.* 62 (2023), e202305639.
- [29] Z. Wu, Z. Xiong, R. Liu, C. He, Y. Liu, Z. Pan, G. Yao, B. Lai, Pivotal roles of N-doped carbon shell and hollow structure in nanoreactor with spatial confined Co species in peroxymonosulfate activation: Obstructing metal leaching and enhancing catalytic stability, *J. Hazard. Mater.* 427 (2022), 128204.
- [30] L. Peng, X. Duan, Y. Shang, B. Gao, X. Xu, Engineered carbon supported single iron atom sites and iron clusters from Fe-rich Enteromorpha for Fenton-like reactions via nonradical pathways, *Appl. Catal. B: Environ.* 287 (2021), 119963.
- [31] P. Duan, J. Pan, W. Du, Q. Yue, B. Gao, X. Xu, Activation of peroxymonosulfate via mediated electron transfer mechanism on single-atom Fe catalyst for effective organic pollutants removal, *Appl. Catal. B: Environ.* 299 (2021), 120714.
- [32] X. Long, Z. Xiong, R. Huang, Y. Yu, P. Zhou, H. Zhang, G. Yao, B. Lai, Sustainable Fe(III)/Fe(II) cycles triggered by co-catalyst of weak electrical current in Fe(III)/peroxymonosulfate system: Collaboration of radical and non-radical mechanisms, *Appl. Catal. B: Environ.* 317 (2022), 121716.
- [33] X. Wang, Z. Xiong, H. Shi, Z. Wu, B. Huang, H. Zhang, P. Zhou, Z. Pan, W. Liu, B. Lai, Switching the reaction mechanisms and pollutant degradation routes through active center size-dependent Fenton-like catalysis, *Appl. Catal. B: Environ.* 457 (2023), 141340.
- [34] R. Zhang, M. Chen, Z. Xu, Y. Guo, B. Lai, Highly efficient degradation of emerging contaminants by magnetic CuO@Fe<sub>3</sub>O<sub>4</sub> derived from natural mackinawite (FeS) in the presence of peroxymonosulfate, *Chin. Chem. Lett.* 33 (2022) 948–952.
- [35] Y. Hong, H. Zhou, Z. Xiong, Y. Liu, G. Yao, B. Lai, Heterogeneous activation of peroxymonosulfate by CoMgFe-LDO for degradation of carbamazepine: Efficiency, mechanism and degradation pathways, *Chem. Eng. J.* 391 (2020), 123604.
- [36] Y. Gao, Y. Zhu, T. Li, Z. Chen, Q. Jiang, Z. Zhao, X. Liang, C. Hu, Unraveling the high-activity origin of single-atom iron catalysts for organic pollutant oxidation via peroxymonosulfate activation, *Environ. Sci. Technol.* 55 (2021) 8318–8328.
- [37] Y. Shang, X. Xu, B. Gao, S. Wang, X. Duan, Single-atom catalysis in advanced oxidation processes for environmental remediation, *Chem. Soc. Rev.* 50 (2021) 5281–5322.
- [38] Y. Shang, X. Duan, S. Wang, Q. Yue, B. Gao, X. Xu, Carbon-based single atom catalyst: synthesis, characterization, DFT calculations, *Chin. Chem. Lett.* 33 (2022) 663–673.
- [39] X. Mi, P. Wang, S. Xu, L. Su, H. Zhong, H. Wang, Y. Li, S. Zhan, Almost 100% Peroxymonosulfate Conversion to Singlet Oxygen on Single-Atom CoN<sub>2+2</sub> Sites, *Angew. Chem. Int. Ed. Engl.* 60 (2021) 4588–4593.
- [40] N. Jiang, H. Xu, L. Wang, J. Jiang, T. Zhang, Nonradical Oxidation of Pollutants with Single-Atom-Fe(III)-Activated Persulfate: Fe(V) Being the Possible Intermediate Oxidant, *Environ. Sci. Technol.* 54 (2020) 14057–14065.
- [41] W. Ma, M. Sun, D. Huang, C. Chu, T. Hedtke, X. Wang, Y. Zhao, J.H. Kim, M. Elimelech, Catalytic membrane with copper single-atom catalysts for effective hydrogen peroxide activation and pollutant destruction, *Environ. Sci. Technol.* 56 (2022) 8733–8745.
- [42] X. Li, X. Huang, S. Xi, S. Miao, J. Ding, W. Cai, S. Liu, X. Yang, H. Yang, J. Gao, J. Wang, Y. Huang, T. Zhang, B. Liu, Single cobalt atoms anchored on porous N-doped graphene with dual reaction sites for efficient Fenton-like catalysis, *J. Am. Chem. Soc.* 140 (2018) 12469–12475.
- [43] Y. Gao, T. Wu, C. Yang, C. Ma, Z. Zhao, Z. Wu, S. Cao, W. Geng, Y. Wang, Y. Yao, Y. Zhang, C. Cheng, Activity trends and mechanisms in peroxymonosulfate-assisted catalytic production of singlet oxygen over atomic metal-N-C catalysts, *Angew. Chem. Int. Ed. Engl.* 60 (2021) 22513–22521.
- [44] Y. Xiong, H. Li, C. Liu, L. Zheng, C. Liu, J.O. Wang, S. Liu, Y. Han, L. Gu, J. Qian, D. Wang, Single-Atom Fe Catalysts for Fenton-Like Reactions: Roles of Different N Species, *Adv. Mater.* 34 (2022), e2110653.
- [45] H. Zhang, H.T. Chung, D.A. Cullen, S. Wagner, U.I. Kramm, K.L. More, P. Zelenay, G. Wu, High-performance fuel cell cathodes exclusively containing atomically dispersed iron active sites, *Energy Environ. Sci.* 12 (2019) 2548–2558.
- [46] X. Liang, D. Wang, Z. Zhao, T. Li, Y. Gao, C. Hu, Coordination number dependent catalytic activity of single-atom cobalt catalysts for Fenton-like reaction, *Adv. Funct. Mater.* 32 (2022) 22030.
- [47] F. Li, G.F. Han, Y. Bu, H.J. Noh, J.P. Jeon, T.J. Shin, S.J. Kim, Y. Wu, H.Y. Jeong, Z. Fu, Y. Lu, J.B. Baek, Revealing isolated M-N<sub>3</sub> C1 active sites for efficient collaborative oxygen reduction catalysis, *Angew. Chem. Int. Ed. Engl.* 59 (2020) 23678–23683.

- [48] C. Zhu, Y. Nie, F. Cun, Y. Wang, Z. Tian, F. Liu, Two-step pyrolysis to anchor ultrahigh-density single-atom FeN<sub>5</sub> sites on carbon nitride for efficient Fenton-like catalysis near 0 °C, *Appl. Catal. B: Environ.* 319 (2022), 121900.
- [49] H. Zhang, J. Li, S. Xi, Y. Du, X. Hai, J. Wang, H. Xu, G. Wu, J. Zhang, J. Lu, J. Wang, A graphene-supported single-atom FeN<sub>5</sub> catalytic site for efficient electrochemical CO<sub>2</sub> reduction, *Angew. Chem. Int. Ed. Engl.* 58 (2019) 14871–14876.
- [50] Z. Song, J. Li, K.D. Davis, X. Li, J. Zhang, L. Zhang, X. Sun, Emerging Applications of Synchrotron Radiation X-Ray Techniques in Single Atomic Catalysts, *Small Methods* 6 (2022), e2201078.
- [51] W. Gu, H. Wang, L. Jiao, Y. Wu, Y. Chen, L. Hu, J. Gong, D. Du, C. Zhu, Single-atom iron boosts electrochemiluminescence, *Angew. Chem. Int. Ed. Engl.* 59 (2020) 3534–3538.
- [52] Y. Li, T. Yang, S. Qiu, W. Lin, J. Yan, S. Fan, Q. Zhou, Uniform N-coordinated single-atomic iron sites dispersed in porous carbon framework to activate PMS for efficient BPA degradation via high-valent iron-oxo species, *Chem. Eng. J.* 389 (2020), 124382.
- [53] Q. Lai, L. Zheng, Y. Liang, J. He, J. Zhao, J. Chen, Metal-organic-framework-derived Fe-N/C electrocatalyst with five-coordinated Fe-N<sub>x</sub> Sites for advanced oxygen reduction in acid media, *ACS Catal.* 7 (2017) 1655–1663.
- [54] L. Chen, Y. Huang, M. Zhou, K. Xing, W. Lv, W. Wang, H. Chen, Y. Yao, Nitrogen-doped porous carbon encapsulating iron nanoparticles for enhanced sulfathiazole removal via peroxymonosulfate activation, *Chemosphere* 250 (2020), 126300.
- [55] C. Tan, N. Gao, Y. Deng, J. Deng, S. Zhou, J. Li, X. Xin, Radical induced degradation of acetaminophen with Fe<sub>3</sub>O<sub>4</sub> magnetic nanoparticles as heterogeneous activator of peroxymonosulfate, *J. Hazard. Mater.* 276 (2014) 452–460.
- [56] X. Liu, P. Shao, S. Gao, Z. Bai, J. Tian, Benzoquinone-assisted heterogeneous activation of PMS on Fe(3)S(4) via formation of active complexes to mediate electron transfer towards enhanced bisphenol A degradation, *Water Res.* 226 (2022), 119218.
- [57] R.-A. DOONG, H.-C. CHIANG, Transformation of carbon tetrachloride by thiol reductants in the presence of quinone compounds, *Environ. Sci. Technol.* 39 (2005) 7460–7468.
- [58] Z.-C. Zhang, F.-X. Wang, F. Wang, C.-C. Wang, P. Wang, Efficient atrazine degradation via photoactivated SR-AOP over S-BUC-21(Fe): the formation and contribution of different reactive oxygen species, *Sep. Purif. Technol.* 307 (2022), 122864.
- [59] C. Guan, J. Jiang, S. Pang, C. Luo, J. Ma, Y. Zhou, Y. Yang, Oxidation kinetics of bromophenols by nonradical activation of peroxydisulfate in the presence of carbon nanotube and formation of brominated polymeric products, *Environ. Sci. Technol.* 51 (2017) 10718–10728.
- [60] S. Wang, X. Zhang, G. Chen, B. Liu, H. Li, J. Hu, J. Fu, M. Liu, Hydroxyl radical induced from hydrogen peroxide by cobalt manganese oxides for ciprofloxacin degradation, *Chin. Chem. Lett.* 33 (2022) 5208–5212.
- [61] Y. Zhou, Y. Lei, Q. Kong, X. Lei, J. Peng, Y. Xie, S. Cheng, Y. Gao, J. Qiu, X. Yang, Reactions of neonicotinoids with peroxydisulfate: The generation of neonicotinoid anion radicals and activation pathway to form sulfate radicals, *J. Hazard. Mater.* 450 (2023), 131081.
- [62] H. Dong, Y. Li, S. Wang, W. Liu, G. Zhou, Y. Xie, X. Guan, Both Fe(IV) and radicals are active oxidants in the Fe(II)/peroxydisulfate process, *Environ. Sci. Technol. Lett.* 7 (2020) 219–224.
- [63] Z. Wang, J. Jiang, S. Pang, Y. Zhou, C. Guan, Y. Gao, J. Li, Y. Yang, W. Qiu, C. Jiang, Is Sulfate Radical Really Generated from Peroxydisulfate Activated by Iron(II) for Environmental Decontamination? *Environ. Sci. Technol.* 52 (2018) 11276–11284.
- [64] J. Yao, N. Wu, X. Tang, Z. Wang, R. Qu, Z. Huo, Methyl phenyl sulfoxide (PMSO) as a quenching agent for high-valent metal-oxo species in peroxymonosulfate based processes should be reconsidered, *Chem. Eng. J. Adv.* 12 (2022), 100378.
- [65] C. Prasse, M. Wagner, R. Schulz, T.A. Ternes, Biotransformation of the antiviral drugs acyclovir and penciclovir in activated sludge treatment, *Environ. Sci. Technol.* 45 (2011) 2761–2769.
- [66] D. Russo, A. Siciliano, M. Guida, E. Galdiero, A. Amoresano, R. Andreozzi, N. M. Reis, G. Li Puma, R. Marotta, Photodegradation and ecotoxicology of acyclovir in water under UV254 and UV254/H<sub>2</sub>O<sub>2</sub> processes, *Water Res.* 122 (2017) 591–602.
- [67] T. An, J. An, Y. Gao, G. Li, H. Fang, W. Song, Photocatalytic degradation and mineralization mechanism and toxicity assessment of antiviral drug acyclovir: Experimental and theoretical studies, *Appl. Catal. B Environ.* 164 (2015) 279–287.
- [68] Y. Wang, X. Zhao, D. Cao, Y. Wang, Y. Zhu, Peroxymonosulfate enhanced visible light photocatalytic degradation bisphenol A by single-atom dispersed Ag mesoporous g-C<sub>3</sub>N<sub>4</sub> hybrid, *Appl. Catal. B Environ.* 211 (2017) 79–88.
- [69] J. Wang, S. Wang, Effect of inorganic anions on the performance of advanced oxidation processes for degradation of organic contaminants, *Chem. Eng. J.* 411 (2021), 128392.
- [70] K. Tian, L. Hu, L. Li, Q. Zheng, Y. Xin, G. Zhang, Recent advances in persulfate-based advanced oxidation processes for organic wastewater treatment, *Chin. Chem. Lett.* 33 (2022) 4461–4477.
- [71] X. Lu, J. Zhao, Q. Wang, D. Wang, H. Xu, J. Ma, W. Qiu, T. Hu, Sonolytic degradation of bisphenol S: effect of dissolved oxygen and peroxydisulfate, oxidation products and acute toxicity, *Water Res.* 165 (2019), 114969.